Optics EXPRESS

Temperature-insensitive directional transverse load sensor based on dual side-hole fiber Bragg grating

JUN HE,[1,2] BAIJIE XU,[1,2] SHUAI JU,[1,2] MAOXIANG HOU,[3] KUIKUI GUO,[1,2] XIZHEN XU,[1,2] YING WANG,[1,2] SHEN LIU,[1,2,4] AND YIPING WANG[1,2,5]

[1] *Key Laboratory of Optoelectronic Devices and Systems of Ministry of Education/Guangdong Province, College of Physics and Optoelectronic Engineering, Shenzhen University, Shenzhen 518060, China*
[2] *Shenzhen Key Laboratory of Photonic Devices and Sensing Systems for Internet of Things, Guangdong and Hong Kong Joint Research Centre for Optical Fibre Sensors, Shenzhen University, Shenzhen 518060, China*
[3] *School of Electromechanical Engineering, Guangdong University of Technology, Guangzhou 510006, China*
[4] *shenliu@szu.edu.cn*
[5] *ypwang@szu.edu.cn*

Abstract: We propose and demonstrate a temperature-insensitive directional transverse load sensor based on a fiber Bragg grating (FBG) inscribed in a section of dual side-hole fiber (DSHF). The application of transverse load results in an effective change in the refractive index and, consequently, changes in the DSHF birefringence. The directional transverse load response of the fabricated DSH-FBG was studied by monitoring the wavelength separations with transverse load applied in different direction with 15° increments. The load sensitivity exhibited two maxima and two minima in a polar coordinate system, achieving a maximum value of 699 pm/(N/mm) for transverse load applied along the slow axis and a minimum value of 285 pm/(N/mm) for transverse load applied along the fast axis. Subsequently, a finite element analysis (FEA) was conducted to simulate the resulting strain distribution of the DSHF with applied directional transverse load. The temperature response of the DSH-FBG transverse load sensor was also tested, yielding a low sensitivity of 1.5×10^{-2} pm/°C. Hence, the compact size, directional transverse load sensitivity, and temperature insensitivity of this device make it suitable for intelligent transverse load monitoring.

1. Introduction

Fiber Bragg gratings (FBGs) are critical elements in a variety of optical fiber systems due to the compact size, narrow bandwidth, immunity to electromagnetic interference, and capability of large-scale multiplexing [1,2]. They are also used for photonic sensors, which are capable of measuring temperature, strain, vibration, and transverse load. FBGs have been inscribed in various fiber types, such as conventional single mode fibers (SMFs) [3–5], micro-structured fibers [6–14], and polarization-maintaining fibers [15–17] for use as transverse load sensors. These FBG devices have been widely used in the measurement of vehicle weight, hydrostatic pressure, and environmental parameters [14,18,19].

Early optical fiber-based transverse load sensor designs primarily consisted of an FBG inscribed in conventional SMF [3]. However, the SM-FBG exhibited a directionless and low sensitivity to transverse load. In recent years, several new transverse load sensors have been demonstrated using FBGs inscribed in micro-structured fibers. The high birefringence of these fibers allows for easy separation of TM and TE modes. For instance, FBGs were successfully inscribed in highly birefringent photonic crystal fiber (Hi-Bi PCF), overcoming the effects of beam scattering

#415082 https://doi.org/10.1364/OE.415082
Journal © 2021 Received 5 Feb 2021; revised 9 May 2021; accepted 12 May 2021; published 24 May 2021

and defocusing caused by air holes [6,7,10,20]. The FBG in a Hi-Bi PCF exhibits wavelength separation sensitivities of 15.3 pm/MPa and ~ 90 pm/(N/mm) to transverse stress and load, respectively [13]. Moreover, the FBG in a special 'butterfly' Hi-Bi PCF exhibits an enhanced transverse load sensitivity of 395 pm/(N/mm) [14]. Additionally, FBGs have also been inscribed in all-solid polarization maintaining fibers (PMFs). Due to the existence of fast and slow axes, FBGs in these PMFs and other Hi-Bi fiber types demonstrate unique directional sensitivity to the applied transverse load [16,17]. For example, the FBG in a PANDA PMF exhibits an angular sensitivity to transverse load. However, the sensitivity in such a PANDA PM-FBG is quite low (~ 16 pm/(N/mm)) [16]. The FBGs in other PMF types, such as bow-tie FMF, can have a higher sensitivity of up to 180 pm/(N/mm) [17]. However, the directional transverse load sensitivity in these Hi-Bi FBGs inscribed in all-solid PMFs is inadequate for transverse load sensing. As such, there is a great interest in developing a novel approach offering simple fabrication and improved directional transverse load sensitivity. Recently, a new dual side-hole fiber (DSHF), which has two air holes in fiber cladding, was proposed and demonstrated for different types of fiber sensors [21–24]. The novel DSHF has a unique stress-induced birefringence property, and hence could potentially be used for developing a directional transverse load sensor.

In this study, we demonstrate the fabrication and use of an FBG in DSHF for directional transverse load sensing. The DSHF includes two air holes with a diameter of 37 µm, a core with a diameter of 8 µm, and a cladding with a diameter of 122 µm. The interval between the two air holes is 51 µm, as shown in Fig. 1. This DSHF exhibits a fiber birefringence on the order of $1{\times}10^{-5}$, a slow axis perpendicular to the two air holes, and a fast axis parallel to the air holes. An FBG was inscribed in the DSHF using a conventional phase mask technique and a UV laser similar to our previous works [25]. The resulting FBG transmission dip features two individual Bragg wavelengths (λ_{TE} and λ_{TM}) corresponding to transverse electric (TE) and transverse magnetic (TM) modes, respectively, induced by the birefringence in the DSH-FBG. The birefringence changes in case the DSHF is subjected to transverse loads [26], leading to a wavelength separation, which exhibits a different sensitivity to the transverse loads applied in different directions.

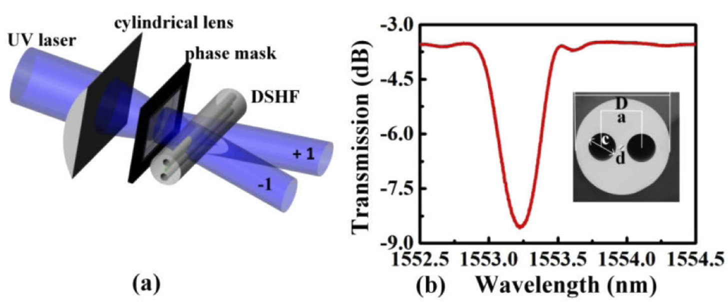

Fig. 1. (a) Schematic diagram of inscribing an FBG in a dual side-hole fiber (DSHF) using the UV laser phase mask method. (b) Transmission spectrum of a fabricated DSH-FBG (Inset: SEM image of the DSHF cross section, which has a core diameter of d = 8 µm, an air hole diameter of c = 37 µm, an interval between two air holes of a = 51 µm, and a cladding diameter of D = 122 µm).

2. Fabrication and demodulation of the proposed DSH-FBG sensor

The schematics of the FBG inscription process is shown in Fig. 1(a). Prior to inscription, the DSHF was hydrogen loaded at 100 °C and 12 MPa for 7 days, to increase the photosensitivity in DSHF. An FBG was inscribed in the hydrogen-loaded DSHF using a conventional phase mask method and a laser source (Coherent, Verdi G-5W) together with a second harmonic generator

Optics EXPRESS

(SHG, Coherent, model MBD). The Verdi laser generated a CW laser beam at a wavelength of 532 nm. The MBD module generated the second harmonic into an ultraviolet (UV) laser at a wavelength of 266 nm [25]. The laser power of 30 mW was employed. As shown in Fig. 1(a), the cylindrical lens has a focal length of 50.2 mm and the phase mask has a grating period of 1070 nm. The efficiency of FBG inscription was affected by the direction of the incident UV laser beam due to the scattering from the air holes. The highest FBG inscription efficiency was achieved in case the incident beam was parallel to the DSHF slow axis. After 100 seconds of UV laser irradiation, the DSH-FBG shows a transmission dip attenuation of −5.4 dB, corresponding to a grating reflectivity of ~69%, as shown in Fig. 1(b).

After grating inscription, the directional transverse load response of the fabricated DSH-FBG was investigated in every direction (from 0° to 360°) with a step of 15°, as shown in Fig. 2. At first, the DSH-FBG was spliced with two SMFs and the transmission spectra of two polarization modes (TE, TM) were measured using a polarization-resolved demodulation system, consisting of a tunable laser (Keysight, 81940A), a polarization synthesizer (Keysight, N7786B), and an optical power meter (Keysight, N7744A). Then, the DSH-FBG was fixed by a pair of rotary fiber holders (Newport, 466A-718) and placed between two parallel glass plates, as shown in Fig. 2(b). Another DSHF with the same fiber diameter was used as a support fiber. The distance between the test fiber and support fiber was ~ 1 cm and the covered length of two fibers was ~ 5 cm. By using these parameters, we could apply uniform transverse load on the DSH-FBG. Subsequently, various transverse loads were applied vertically to the upper plate using a pressure gauge (HLD, Handpi Instruments), in which the applied transverse load could be detected and controlled precisely. The orientation of applied transverse load could be changed by simultaneously rotating the rotary fiber holders. By this means, fiber twisting could be avoided during the transverse load measurements. Note that the initial angular alignment for DSHF ($\theta = 0°$, i.e. along the fast axis) was conducted via a CCD camera. Before the transverse load was applied on the DSH-FBG, the fiber orientation was examined based on the CCD-captured top-view microscope images of the test DSH-FBG. In specific, a minimum shadow width of the holes will be observed in the case of $\theta = 0°$, i.e. along the fast axis.

As shown in Fig. 2(b), the polarization-resolved transmission spectra are obtained using a Mueller method, which is a deterministic method that derives the FBG transmission spectra in two polarizations from its Mueller matrix. The input light of the FBG can be characterized by the Stokes vector S_{in}, interacts with the DSH-FBG, and generates output light with a Stokes vector S_{out}. The wavelength-dependent polarization transmission properties of the DSH-FBG are denoted by a 4×4 matrix $M(\lambda)$ (i.e., the Mueller matrix) as

$$S_{out}(\lambda) = M(\lambda) \times S_{in}(\lambda). \tag{1}$$

Only the first row coefficients $m_{11}(\lambda)$, $m_{12}(\lambda)$, $m_{13}(\lambda)$, and $m_{14}(\lambda)$ of the Mueller matrix are required since S_{0out} (λ) represents the total output optical power at the wavelength λ, and can be expressed as

$$\begin{aligned} P_{out}(\lambda) &= S_{0out}(\lambda) \\ &= m_{11}(\lambda) \cdot S_{0in}(\lambda) + m_{12}(\lambda) \cdot S_{1in}(\lambda) + m_{13}(\lambda) \cdot S_{2in}(\lambda) + m_{14}(\lambda) \cdot S_{3in}(\lambda). \end{aligned} \tag{2}$$

Four well-defined polarization states, i.e. at linear horizontal (P_{LH}), linear vertical (P_{LV}), linear diagonal (P_{LD}, i.e. +45°), and right-hand circular polarization (P_{RC}), are generated using the polarization synthesizer. The transmission spectra of FBG are measured for each polarization state, producing four wavelength-dependent arrays of input power [P_a (λ), P_b (λ), P_c (λ), P_d (λ)] as the reference and four wavelength-dependent arrays of output power [P_1 (λ), $P_2(\lambda)$, $P_3(\lambda)$,

Optics EXPRESS

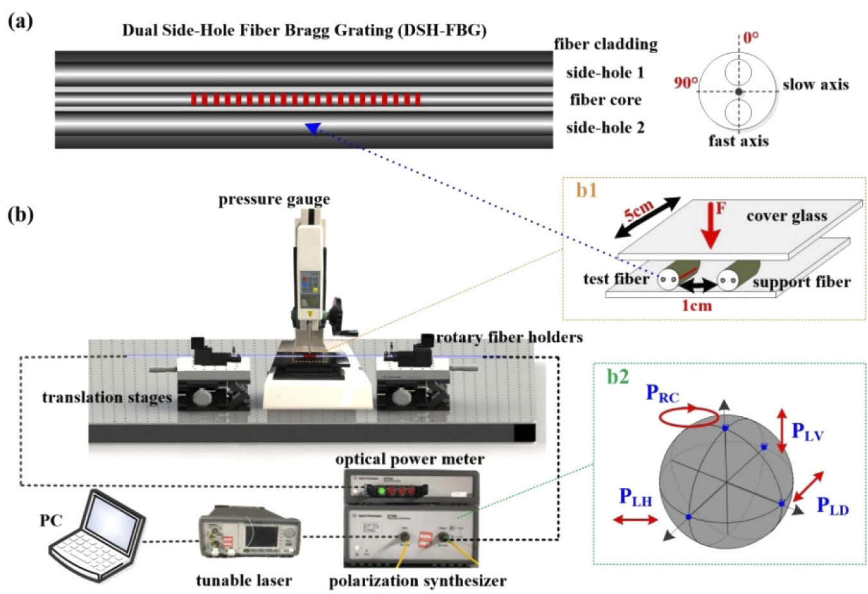

Fig. 2. (a) Schematics of the proposed DSH-FBG sensor. (b) Experimental setup for testing the directional transverse load response of the proposed DSH-FBG sensor. (Inset b1, the application of lateral force F and corresponding transverse load on the test fiber (DSH-FBG sensor). Inset b2, generation of 4 different polarization states on the Poincaré sphere for Mueller matrix-based polarization-resolved measurement.)

$P_4(\lambda)$]. Equation (2) can be rewritten for all four polarization states as

$$\begin{cases} P_1(\lambda) = m_{11}(\lambda) \cdot P_a(\lambda) + m_{12}(\lambda) \cdot P_a(\lambda) \\ P_2(\lambda) = m_{11}(\lambda) \cdot P_b(\lambda) + m_{12}(\lambda) \cdot P_b(\lambda) \\ P_3(\lambda) = m_{11}(\lambda) \cdot P_c(\lambda) + m_{13}(\lambda) \cdot P_c(\lambda) \\ P_4(\lambda) = m_{11}(\lambda) \cdot P_d(\lambda) + m_{14}(\lambda) \cdot P_d(\lambda) \end{cases}. \tag{3}$$

Solving these equations, the first row coefficients of the Mueller matrix are obtained as

$$\begin{bmatrix} m_{11}(\lambda) \\ m_{12}(\lambda) \\ m_{13}(\lambda) \\ m_{14}(\lambda) \end{bmatrix} = \begin{bmatrix} \frac{1}{2}\left(\frac{P_1(\lambda)}{P_a(\lambda)} + \frac{P_2(\lambda)}{P_b(\lambda)}\right) \\ \frac{1}{2}\left(\frac{P_1(\lambda)}{P_a(\lambda)} - \frac{P_2(\lambda)}{P_b(\lambda)}\right) \\ \frac{P_3(\lambda)}{P_c(\lambda)} - m_{11}(\lambda) \\ \frac{P_4(\lambda)}{P_d(\lambda)} - m_{11}(\lambda) \end{bmatrix}. \tag{4}$$

The transmission spectra of the DSH-FBG can be determined by

$$T(\lambda) = \frac{P_{out}(\lambda)}{P_{in}(\lambda)} = \frac{S_{0out}(\lambda)}{S_{0in}(\lambda)} = m_{11}(\lambda) + \frac{m_{12}(\lambda) \cdot S_{1in}(\lambda) + m_{13}(\lambda) \cdot S_{2in}(\lambda) + m_{14}(\lambda) \cdot S_{3in}(\lambda)}{S_{0in}(\lambda)}. \tag{5}$$

The extreme of transmission spectra, measured at two orthogonal polarization states (TE and TM) of an optical fiber device, can be derived as

$$\begin{aligned} T_{\max}(\lambda) &= m_{11}(\lambda) + \sqrt{(m_{12}(\lambda))^2 + (m_{13}(\lambda))^2 + (m_{14}(\lambda))^2} \\ T_{\min}(\lambda) &= m_{11}(\lambda) - \sqrt{(m_{12}(\lambda))^2 + (m_{13}(\lambda))^2 + (m_{14}(\lambda))^2} \end{aligned}. \tag{6}$$

Moreover, the application of transverse load can induce changes in the fiber birefringence, resulting in a shift in the FBG peaks λ_{TE} and λ_{TM}, corresponding to resonance dips of the TE and TM polarizations, respectively. Additionally, the effective birefringence of the DSHF B can be expressed as

$$B = |n_{TE} - n_{TM}| = \left|\frac{\lambda_{TE} - \lambda_{TM}}{2\Lambda_B}\right|, \tag{7}$$

where n_{TE} and n_{TM} are the effective indices for the TE and TM modes, respectively. The FBG period is denoted by Λ_B.

3. Directional transverse load response of the DSH-FBG sensor

At first, we studied the transmission spectra evolution of a DSH-FBG with increasing transverse load applied at two specific directions, i.e. along the slow axis ($\theta = 90°$) and fast axis ($\theta = 0°$), respectively. In case an increasing transverse load was applied on the DSH-FBG along the slow axis ($\theta = 90°$), as shown in Figs. 3(a) and 3(c), the Bragg resonance dip in the transmission spectrum gradually split into two individual dips, corresponding to resonance dips of the TE and TM modes (λ_{TE} and λ_{TM}), respectively. As shown in Fig. 3(c), as the transverse load increased, the TE mode dip λ_{TE} shifted toward shorter wavelengths, whereas the TM mode dip λ_{TM} shifted toward longer wavelengths. In the absence of transverse load (0 N/mm), the dip wavelengths were measured to be $\lambda_{TE} = 1553.220$ nm and $\lambda_{TM} = 1553.290$ nm. Hence, the wavelength separation $\Delta\lambda$ between dip wavelengths λ_{TM} and λ_{TE} was 70 pm, and the initial birefringence B_o of the DSHF was calculated to be 6.54×10^{-5} using Eq. (7). When the transverse load was increased to 0.7 N/mm, the dip wavelengths were measured to be $\lambda_{TE} = 1552.912$ nm and $\lambda_{TM} = 1553.498$ nm, the wavelength separation $\Delta\lambda$ between λ_{TM} and λ_{TE} was 586 pm, and the calculated birefringence B increased to 5.48×10^{-4}. Furthermore, in case an increasing transverse load was applied on the DSH-FBG along the fast axis ($\theta = 0°$), as shown in Fig. 3(b), the Bragg resonance dip was distorted in accompany with a deceased dip attenuation, resulting from the asynchronous transmission spectra evolutions of the TE- and TM- modes. As shown in Fig. 3(d), both the TE- and TM- mode dips shifted to shorter wavelengths with an increasing transverse load. However, the wavelength shift in TE mode was larger than that in TM mode. When the transverse load was increased to 0.7 N/mm, mode wavelengths were measured to be $\lambda_{TE} = 1552.970$ nm and $\lambda_{TM} = 1553.236$ nm, the wavelength separation $\Delta\lambda$ between λ_{TM} and λ_{TE} was 266 pm, and the birefringence increased to 2.49×10^{-4}. Note that the transmission spectra of DSH-FBG evolve differently with the same amount of transverse load applied along the slow axis and fast axis. Additionally, the transverse load applied along the slow axis could introduce a much larger birefringence ($B = 5.48 \times 10^{-4}$) than that applied along the fast axis ($B = 2.49 \times 10^{-4}$).

Furthermore, the dip wavelength of the TE- and TM- modes (λ_{TE} and λ_{TM}) of DSH-FBG were extracted from Figs. 3(c) and 3(d) and plotted in Fig. 4 as functions of the increasing transverse load applied along the slow axis ($\theta = 90°$) and fast axis ($\theta = 0°$). Moreover, the wavelength separation $\Delta\lambda$ between λ_{TE} and λ_{TM} was also calculated. Linear fits were applied to all shifts in the two Bragg wavelengths (λ_{TE}, λ_{TM}) and wavelength separation $\Delta\lambda$. The DSH-FBG exhibited a wavelength sensitivity (represented by the slope of the linear fit) of 699 pm/(N/mm) along the slow axis ($\theta = 90°$) and 285 pm/(N/mm) along the fast axis ($\theta = 0°$). In contrast, the changes in DSHF birefringence were larger when the slow axis was stressed by a transverse load, while the changes were smaller along the fast axis. These results suggest that the wavelength shifts exhibit different responses depending heavily on the directionality.

We further investigated the directional transverse load response of the DSH-FBG in every direction (from 0° to 360°) with a step of 15°. At each orientation angle θ, the dip wavelength of the TE- and TM- modes (λ_{TE} and λ_{TM}) of the DSH-FBG were recorded as functions of the applied transverse load. Moreover, sensitivities were obtained from wavelength separation $\Delta\lambda$ between λ_{TE} and λ_{TM} at different directions and are displayed in polar coordinates in Fig. 5. It

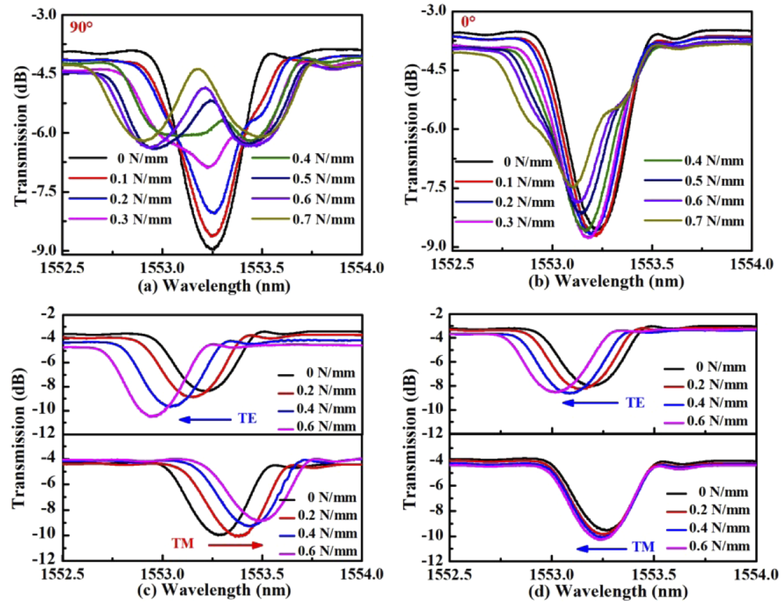

Fig. 3. Transmission spectra evolutions of the fabricated DSH-FBG with increasing transverse load applied along the (a) slow axis (θ = 90°) and (b) fast axis (θ = 0°). Also shown are the transmission spectra evolutions of the TE- and TM-modes with increasing transverse load applied along the (c) slow axis (θ = 90°) and (d) fast axis (θ = 0°).

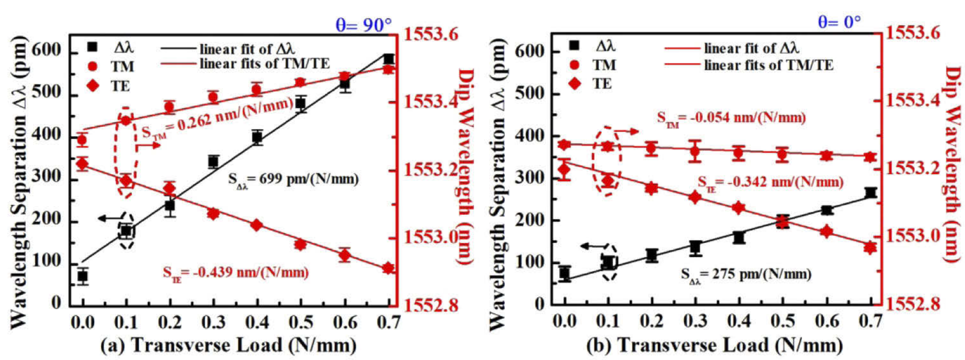

Fig. 4. The dip wavelength of the TE- and TM- modes (λ_{TE} and λ_{TM}) of the DSH-FBG and the corresponding wavelength separation Δλ as functions of an increasing transverse load applied along the (a) slow axis (θ = 90°) and (b) fast axis (θ = 0°).

Optics EXPRESS

is obvious that the transverse load sensitivity exhibits a strong angular dependence, i.e., the sensitivity reaches maximum values at 90° and 270° (transverse load applied along the slow axis) and minimum values at 0° and 180° (transverse load applied along the fast axis). We also measured the directional transverse load response of an FBG inscribed in a conventional SMF by using the same method. The results are also demonstrated in Fig. 5 for comparison. The SM-FBG exhibits a low sensitivity of 200 pm/(N/mm), less than the minimum sensitivity of DSH-FBG (285 pm/(N/mm)). Moreover, no significant angular dependence could be observed in the response of the SM-FBG sensitivities. These results suggest the presence of two large air holes in DSHF could effectively increase the sensitivity of the birefringence in a cylindrical fiber when subjected to a transverse load.

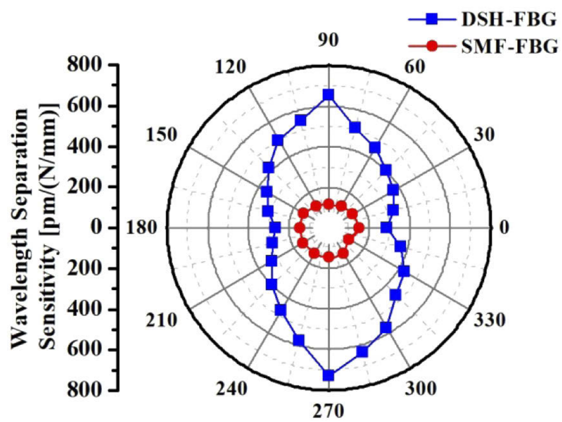

Fig. 5. Directional transverse load response of a DSH-FBG and an SM-FBG in every direction (from 0° to 360°) with a step of 15° (i.e. wavelength separation sensitivities of the DSH-FBG and SM-FBG to transverse load as functions of orientation angle θ displayed in polar coordinates).

The birefringence in DSH-FBG varied due to photoelastic effects [27]. When the grating was subjected to transverse load, the induced stress produced a change in the refractive index, which shifted the transmission spectra of the TE- and TM- modes. The refractive index of pure silica subjected to transverse load is given by [28]

$$n_{TE} = n_0 - C_1\sigma_z - C_2(\sigma_y + \sigma_x), \tag{8}$$

$$n_{TM} = n_0 - C_1\sigma_y - C_2(\sigma_z + \sigma_x), \tag{9}$$

where n_0 represents the refractive index of fused silica without applied pressure. The terms σ_x, σ_y, and σ_z are the directional stress components, while $C_1 = 6.5\times10^{-13}$ m^2/N and $C_2 = 4.2\times10^{-12}$ m^2/N are photoelastic coefficients for pure silica. In this study, the x-axis was the fiber axis, the y-axis was the fast axis ($\theta = 0°$), and the z-axis was the slow axis ($\theta = 90°$), as shown in Fig. 6.

Subsequently, a finite element analysis (FEA) was conducted in ANSYS using the same parameters for the cross section of a DSHF. Simulation parameters for silica were set as follows, i.e., Young's modulus of 73 GPa, Poisson's ratio of 0.17, and the density of 2700 kg/m^3 [5]. Figure 6 shows the simulated stress contour profiles of the DSHF under an applied pressure of 1 MPa (i.e., a lateral force of ~2.4 N acting on the circumferential arc surface corresponding to 22.5°). The blue and red areas represent minimum and maximum stress values, respectively. In case the pressure of 1 MPa was applied on the DSHF along the slow axis ($\theta = 90°$), as shown in Figs. 6(a) and 6(b), the stress in y-direction are positive, whereas the stress in z-direction are negative. The force applied along the slow axis ($\theta = 90°$) can induce different stress in two

Optics EXPRESS

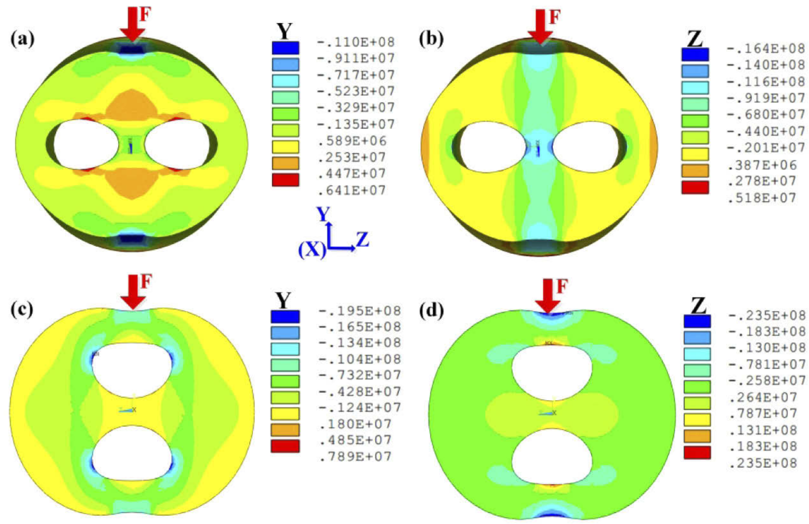

Fig. 6. A finite element analysis (FEA) diagram of the DSHF with transverse load (lateral force) applied along the (a), (b) slow axis (θ = 90°), and (c), (d) fast axis (θ = 0°). (a) and (c) represent the stress distribution along y-direction, (b) and (d) represent the stress distribution along z-direction.

orthogonal axes of the DSHF. Hence, different refractive index changes are introduced through photoelastic effects [27], resulting in different wavelength shifts, i.e., the 'blue' shift and 'red' shift of TE- and TM- modes (as shown in Figs. 3 and 4). Moreover, in case the pressure of 1 MPa was applied on the DSHF along the slow axis (θ = 0°), as shown in Figs. 6(c) and 6(d), both the stress in *y*-direction and *z*-direction are negative, and hence result in similar 'blue' shifts of TE- and TM- modes (as shown in Figs. 3 and 4). The results show that external pressure can produce a stress concentration in the applied area, which is then transferred to the air holes of DSHF. Any changes in the refractive index of silica were caused by photoelastic effects, which led to variations in the birefringence and wavelength shifts. Note that the maximum amount of stress produced by the lateral forces applied along the slow axis (19.5×10^7 Pa) is larger than that achieved along the fast axis (11×10^7 Pa). This indicates the transverse loads applied along the slow axis will produce larger birefringence changes. As a result, the simulation results are in consistence with the previous experimental results.

4. Temperature response of the DSH-FBG sensor

We also investigated the temperature response of the DSH-FBG transverse load sensor. The DSH-FBG was placed in an oven, and the transmission spectra of TE- and TM- modes were recorded with an increasing temperature from room temperature to 75 °C. Figure 7(a) shows the transmission spectra evolutions of the TE- and TM- modes with an increasing temperature. As shown in Fig. 7(b), the dip wavelength of the TE- and TM- modes (λ_{TE} and λ_{TM}) exhibit similar 'red' shifts with almost the same temperature sensitivity of 11.73 and 11.75 pm/°C, closed to the sensitivity of a conventional SM-FBG. However, the wavelength separation Δλ between λ_{TE} and λ_{TM} remains almost constant with increasing temperature. As shown in Fig. 7(b), standard variations in the wavelength separation Δλ are less than 1 pm in the temperature range from 20 to 75°C. The wavelength sensitivity to temperature is as low as -1.5×10^{-2} pm/°C. In other words, the birefringence and corresponding wavelength separation Δλ in the DSH-FBG transverse load sensor is insensitive to temperature variations.

Optics EXPRESS

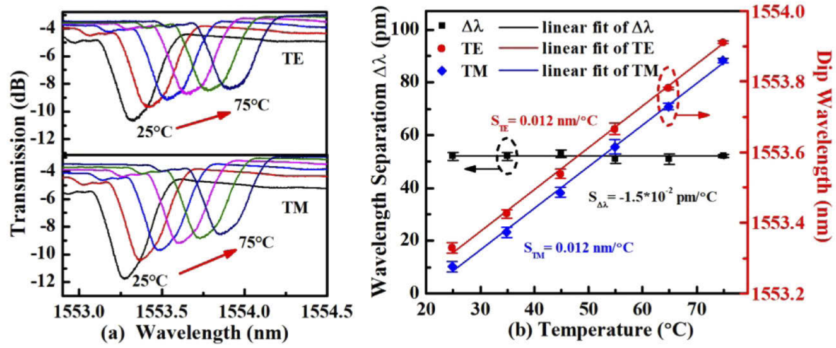

Fig. 7. (a) Transmission spectra evolutions of the TE- and TM- modes with an increasing temperature. (b) The dip wavelength of the TE- and TM- modes of the DSH-FBG and wavelength separation Δλ as functions of the increasing temperature.

5. Conclusion

We have reported a novel directional transverse load sensor utilizing an FBG inscribed in a DSHF. The stress induced by transverse load produced changes in refractive index, variations in DSHF birefringence, and a shift in the transmission spectrum. The transverse load response was investigated in all directions (0° to 360°) with a step of 15°. Strong angular dependence was observed in the DSHF-FBG sensitivity, achieving a maximum of 699 pm/(N/mm) and a minimum of 285 pm/(N/mm). This maximum occurred with transverse load applied along the slow axis, while the minimum occurred with transverse load applied along the fast axis. The FEA simulation results of transverse load-induced stress distributions also supported this conclusion. Moreover, the sensitivity of the DSH-FBG to transverse load was higher than that of an SM-FBG. The proposed DSH-FBG sensors exhibit several advantages such as compact structure, directional transverse load sensitivity, and temperature insensitivity. These qualities make it a promising new tool for high-performance transverse load measurements in many applications, such as advanced robots and intelligent transportations.

Funding. National Natural Science Foundation of China (U1913212, 61875128, 61635007); Guangdong Science and Technology Department (2019TQ05X113, 2019A1515011393, 2019B1515120042); Shenzhen Science and Technology Innovation Program (RCYX20200714114538160, JCYJ20170818143853289, JCYJ20180507182058432); China Postdoctoral Science Foundation (2019M663049).

Disclosures. The authors declare no conflicts of interest.

References

1. C. R. Giles, "Lightwave applications of fiber Bragg gratings," J. Lightwave Technol. **15**(8), 1391–1404 (1997).
2. Y. J. Rao, "Recent progress in applications of in-fiber Bragg grating sensors," Opt. Lasers Eng. **31**(4), 297–324 (1999).
3. R. Aashia, K. V. Madhav, B. Srinivasan, and S. Asokan, "Strain-temperature discrimination using a single fiber Bragg grating," IEEE Photonics Technol. Lett. **22**(11), 778–780 (2010).
4. H. B. Liu, H. Y. Liu, G. D. Peng, and P. L. Chu, "Strain and temperature sensor using a combination of polymer and silica fiber Bragg gratings," Opt. Common. **219**(1-6), 139–142 (2003).
5. J. He, Y. P. Wang, C. R. Liao, Q. N. Wang, K. M. Yang, B. Sun, G. L. Yin, S. Liu, J. T. Zhou, and J. Zhao, "Highly birefringent phase-shifted fiber Bragg gratings inscribed with femtosecond laser," Opt. Lett. **40**(9), 2008–2011 (2015).
6. F. Berghmans, T. Geernaert, T. Baghdasaryan, and H. Thienpont, "Challenges in the fabrication of fibre Bragg gratings in silica and polymer microstructured optical fibres," Laser Photon. Rev. **8**(1), 27–52 (2014).
7. T. Geernaert, M. Becker, P. Mergo, T. Nasilowski, J. Wójcik, W. Urbanczyk, M. Rothhardt, C. Chojetzki, H. Bartelt, H. Terryn, F. Berghmans, and H. Thienpont, "Bragg grating inscription in GeO_2-doped microstructured optical fibers," J. Lightwave Technol. **28**(10), 1459–1467 (2010).
8. M. X. Hou, K. M. Yang, J. He, X. Z. Xu, S. Ju, K. K. Guo, and Y. P. Wang, "Two-dimensional vector bending sensor based on seven-core fiber Bragg gratings," Opt. Express **26**(18), 23770–23781 (2018).

Optics EXPRESS

9. C. Jewart, K. P. Chen, B. McMilen, M. M. Bails, S. P. Levitan, J. Cannng, and I. V. Avdeev, "Sensitivity enhancement of fiber Bragg gratings to transverse stress by using microstructural fibers," Opt. Lett. **31**(15), 2260–2262 (2006).
10. T. Geernaert, K. Kalli, C. Koutsides, M. Komodromos, T. Nasilowski, W. Urbanczyk, J. Wojcik, F. Berghmans, and H. Thienpont, "Point-by-point fiber Bragg grating inscription in free-standing step-index and photonic crystal ibers using near-IR femtosecond laser," Opt. Lett. **35**(10), 1647–1649 (2010).
11. Z. Y. Liu, C. Wu, M. L. V. Tse, C. Lu, and H. Y. Tam, "Ultrahigh birefringence index-guiding photonic crystal fiber and its application for pressure and temperature discrimination," Opt. Lett. **38**(9), 1385–1387 (2013).
12. T. Tenderenda, K. Skorupski, M. Makara, G. S. Barabach, P. Mergo, P. Marc, L. R. Jaroszewic, and T. Nasilowski, "Highly birefringent dual-mode microstructured fiber with enhanced polarimetric strain sensitivity of the econd order mode," Opt. Express **20**(24), 26996–27002 (2012).
13. T. Geernaert, G. Luyckx, E. Voet, T. Nasilowski, K. Chah, M. Becker, H. Bartelt, W. Urbanczyk, J. Wojcik, W. D. Waele, J. Degrieck, H. Terryn, F. Berghmans, and H. Thienpont, "Transversal load sensing with fiber Bragg gratings in microstructured optical fibers," IEEE Photonics Technol. Lett. **21**(1), 6–8 (2009).
14. C. Sonnenfeld, S. Sulejmani, T. Geernaert, S. Eve, N. Lammens, G. Luyckx, E. Voet, J. Degrieck, W. Urbanczyk, P. Mergo, M. Becker, H. Bartelt, F. Berghmans, and H. Thienpont, "Microstructured optical fiber sensors embedded in a laminate composite for smart material applications," Sensors **11**(3), 2566–2579 (2011).
15. T. Feng, D. L. Ding, Z. H. Li, and X. S. Yao, "First quantitative determination of birefringence variations indued by axial-strain in polarization maintaining fibers," J. Lightwave Technol. **35**(22), 4937–4942 (2017).
16. J. F. B. Cadavid, J. D. C. Buelvas, and P. Torres, "Spectral properties of locally pressed fiber Bragg gratings written in polarization maintaining fibers," J. Lightwave Technol. **28**(9), 1291–1297 (2010).
17. E. Chehura, C. C. Ye, S. E. Staines, S. W. James, and R. P. Tatam, "Characteriation of the fiber Bragg gratings fabricated in stress and geometrically induced high birefringence fibers to temperature and transverse load," Smart Mater. Struct. **13**(4), 888–895 (2004).
18. S. Sulejmani, C. Sonnenfeld, T. Geernaert, P. Mergo, M. Makara, K. Poturaj, K. Skorupski, T. Martynkien, G. Satkiewicz-Barabach, J. Olszewski, W. Urbanczyk, C. Caucheteur, K. Chah, P. Megret, H. Terryn, J. V. Roosbroeck, F. Berghmans, and H. Thienpont, "Control over the pressure sensitivity of Bragg grating-based sensors in highly birefringent microstructured optical fibers," IEEE Photonics Technol. Lett. **24**(6), 527–529 (2012).
19. S. Sulejmni, C. Sonnenfeld, T. Geernat, G. Luyckx, D. V. Hemelrick, P. Mergo, W. Urbanczy, K. Chah, P. Megret, H. Thienpont, and F. Berghmans, "Sheer stress sensing with Bragg grating-based sensors in micro-structured optical fibers," Opt. Express **21**(17), 20404–20416 (2013).
20. R. Goto, I. Fsaifes, A. Baz, L. Bigot, K. Takenaga, S. Matsuo, and S. D. Jackson, "UV-induced Bragg grating inscription into single-polarization all-solid hybrid mirostructured optical fiber," Opt. Express **19**(14), 13525–13530 (2011).
21. E. Chmieleska, W. Urbanczyk, and W. J. Bock, "Measurement of pressure and temperature sensitivities of a Bragg grating imprinted in a highly birefringent side-hole fiber," Appl. Opt. **42**(31), 6284–6291 (2003).
22. S. Wu, G. Yan, B. Zhou, E. H. Lee, and S. He, "Open-cavity Fabry-Perot interferometer based on etched side-hole fiber for microfluidic sensing," IEEE Photonics Technol. Lett. **27**(17), 1813–1816 (2015).
23. Y. L. Xiu, K. R. Wang, B. B. Yan, Y. H. Luo, J. H. Yuan, C. X. Yu, H. F. Qi, L. W. Yang, C. Wang, and G. D. Peng, "Refractive index sensor based on multimode interference in a twin-hole fiber," Opt. Eng. **59**(09), 097102 (2020).
24. S. Li and Y. Zhao, "A Mach-Zehnder interferometer based on tapered dual side hole fiber for refractive index sensing," Opt. Fiber Technol. **45**, 267–270 (2018).
25. J. T. Zhou, K. K. Guo, J. He, M. X. Hou, Z. Zhang, C. R. Liao, Y. Wang, G. X. Xu, and Y. P. Wang, "Novel fabrication technique for phase-shifted fiber Bragg gratings using a variable-velocity scanning beam and a shielded phase mask," Opt. Express **26**(10), 13311–13321 (2018).
26. R. B. Wagreich, W. A. Atia, H. Singh, and J. S. Sirkis, "Effects of diametric load on fibre Bragg gratings fabricated in low birefringent fibre," Electron. Lett. **32**(13), 1223–1224 (1996).
27. R. Gafsi and M. A. El-Sherif, "Analysis of induced-birefringence effects on fiber Bragg gratings," Opt. Fiber Technol. **6**(3), 299–323 (2000).
28. C. R. Dennison and P. M. Wild, "Sensitivity of Bragg gratings in birefringent optical fiber to transverse compression between conforming materials," Appl. Opt. **49**(12), 2250–2261 (2010).